Size and density controlled deposition of Ag nanoparticle films by a novel low temperature spray chemical vapour deposition method – research into mechanism, particle growth and optical simulation

Yang Liu[a,b]†*, Paul Plate[a]†*, Volker Hinrichs[a], Tristan Köhler[a], Min Song[a], Phillip Manley[a], Martina Schmid[a,c], Peter Bartsch[d], Sebastian Fiechter[a], Martha Ch. Lux-Steiner[a], Christian-Herbert Fischer[b]

a. Helmholtz-Zentrum Berlin für Materialien und Energie GmbH, Hahn-Meitner-Platz 1, 14109 Berlin, Germany.
b. Institute of Chemistry and Biochemistry, Freie Universität Berlin, Fabeckstr. 34-36, 14195 Berlin, Germany.
c. Department of Physics, Freie Universität Berlin, Arnimallee 14, 14195 Berlin, Germany.
d. Fachbereich VIII Maschinenbau, Veranstaltungstechnik, Verfahrenstechnik, Beuth Hochschule für Technik Berlin, Luxemburger Str. 10, 13353 Berlin, Germany
† These authors contributed equally to the work.
* E-mail: yang.liu@helmholtz-berlin.de; paul.plate@helmholtz-berlin.de

Abstract   Ag nanoparticles have attracted interest for plasmonic absorption enhancement of solar cells. For this purpose well-defined particle sizes and densities as well as very low deposition temperatures are required. Thus, we report here a new spray chemical vapour deposition method for producing Ag NP films with independent size and density control at substrate temperatures even below 100 °C which is much lower than for many other techniques. This method can be used on different substrates to deposit Ag NP films. It is a reproducible, low-cost process which uses Trimethylphosphine (hexafluoroacetylacetonato) silver as precursor in alcoholic solution. By systematic variation of deposition parameters and classic experiments, mechanisms of particle growth and of deposition processes as well as the low decomposition temperature of the precursor could be explained. Using the 3D finite element method, absorption spectra of selected samples were simulated which fitted well with the measured results. Hence, further applications of such Ag NP films for generating plasmonic near field can be predicted by the simulation.

Keywords silver nanoparticle film; plasmonic nanoparticle; size and density control; aerosol assisted chemical vapour deposition; mechanism of deposition process

Introduction

In recent years, research on plasmonic enhancement of solar cells has attracted high interest (Atwater and Polman, 2010; Ferry et al., 2011; Ferry et al., 2010; van Lare et al., 2015; Yue et al., 2016). The implementation of plasmonic nanostructures can cause absorption enhancement of different kinds of solar cell absorbers which allows either decreasing the physical thickness of an absorber layer while keeping the optical thickness constant, e.g., for $Cu(In,Ga)Se_2$, CdTe, or improving absorption in poorly absorbing materials like Si (Atwater and Polman, 2010). Therefore, for the first condition it is advantageous for reducing the consumption of scarce elements such as indium and telluride in the absorber layer as well as decreasing the cost of the devices. Among the well-studied plasmonic nanostructures, silver nanoparticles (Ag NPs) have been widely used in several types of solar cells, e.g., thin film silicon solar cells (Chen et al., 2012; van Lare et al., 2012), thin film $Cu(In,Ga)Se_2$ solar cells (Schmid et al., 2013; Yin et al., 2015), organic solar cells (Kalfagiannis et al., 2012; Kim et al., 2008) and perovskite solar cells (Qian et al., 2015; Yue et al., 2016). Silver shows a plasmonic resonance in the visible and the near-infrared range of the spectrum. By tuning the Ag NPs' size, geometry, density and surrounding medium, the resonance peak can be shifted in a controlled way between 300 and 1200 nm (Cobley et al., 2009; Mock et al., 2002). Ag NPs are also utilized for surface enhanced Raman spectroscopy (Wang and Rothberg, 2006). In this application, controlled particle sizes and a good homogeneity of the particle films are crucial (Moskovits, 2005; Nie and Emory, 1997). Moreover, for low thermal stability absorber layers like the new, promising perovskite (Berhe et al., 2016), it is necessary to deposit Ag NPs at a low substrate temperature.

Ag NP films can be obtained by different approaches. The most common one is the colloidal route, e.g., the preparation of colloidal Ag NPs by reducing a silver salt like silver nitrate (Murphy et al., 2015). By using different surfactants, size and geometry of the Ag NPs could be controlled (Abou El-Nour et al., 2010; Pelton et al., 2008). Laser ablation techniques are also suitable for the preparation of colloidal Ag NPs (Valverde-Alva et al., 2015). The drawback of colloidal methods is that a second step is needed for depositing and fixing the particles on a substrate. A simpler method is that of annealing thin evaporated silver film which can also form Ag NPs (Schmid et al., 2013). Atomic layer deposition is able to deposit Ag NPs directly at temperatures lower than 110 °C (Masango et al., 2014). In both cases, costly low pressure or vacuum equipment is needed. A promising approach is the spray pyrolysis method. It is widely used for preparing a variety of compact films and also nanoparticles on different substrates (Fu et al., 2016; Fu et al., 2013; Perednis and Gauckler, 2005; Teoh et al., 2010). Ag NPs can be deposited by spray pyrolysis using silver nitrate as precursor material, but a substrate temperature higher than 400 °C is required (Kumar et al., 2014; Pingali et al., 2005; Pluym et al., 1993; Shih and Chien, 2013). This high temperature is not suitable for the incorporation of Ag NPs into solar cells. Above all, a low temperature deposition method which can also control the size and density of Ag NPs is required.

In this work, a new aerosol assisted deposition method of Ag NPs is shown. An ultrasonic humidifier is used for generating the aerosol. This low cost spray chemical vapour deposition (spray-CVD) method is adapted from the ILGAR[®] process (ion layer gas reaction) and operates under atmospheric pressure.(Fischer et al., 2011; Liu et al., 2015) Trimethylphosphine (hexafluoroacetylacetonato) silver (Ag(hfacac)PMe$_3$) was used as precursor to form Ag NPs on fluorine-doped tin oxide coated glass substrates (FTO). By varying different deposition parameters, size and density controlled Ag NP films can be obtained. For most of the Ag NPs samples, only a substrate temperature of 110 °C temperature is needed, which is much lower than many other methods. Size, density and deposition rate of Ag NPs were mainly investigated by scanning electron microscopy (SEM) and laser ablation inductively coupled plasma mass spectrometry (LA-ICP-MS). The deposition mechanism of the process is studied in detail based on variation of substrate temperature and additional classical chemical experiments. Optical properties and related simulations of selected Ag NP films were studied to better understand the potential applications.

Results and discussion

Development of Ag nanoparticle films at 110 °C and 230 °C

First we will show how Ag nanoparticle films develop during the spray chemical vapour deposition. The aerosol of a 10 mM alcoholic Ag(hfacac)PMe$_3$ solution was blown towards the heated FTO substrate (Fig. 1). Thereby solvent and subsequently precursor evaporate and the latter decomposes to solid Ag NPs on the substrate. Fig. 2 shows the SEM images of Ag NP films with deposition times from 0.5 min to 15 min at a substrate temperature of 110 °C. The large grains are FTO. With increasing deposition time up to 7.5 min, the small Ag NPs grow bigger and keep separated. From 10 min on, Ag NPs start to touch each other or grow on a neighbouring particle. At all times the particles are relatively mono-dispersed. They are not ideally spherical, but have edges, some exhibit clear geometric shapes like triangles or icosahedra. A closer inspection shows that at least during the first 5min the particles form preferentially within FTO valleys.

From SEM images, the Ag NPs obtained at 230 °C substrate temperature look quite different (Fig. 3). Due to higher reaction rate the material yield, coverage and density are bigger. The particle size is smaller; because of high nucleation rate the incoming material is distributed on many more species. The generally increased poly-dispersity and from 10 min more frequent aggregation and multi-layer structures are striking, but the original particles are still visible, i.e., they are not fused completely. Also the grains in a higher level are not merged. Obviously, big particles which are grown quickly in a position inappropriate for crystal fusion are not able anymore to rearrange at 230 °C. The deposition seems favoured on the surface of

already existing big particles rather than forming new nuclei between the Ag NPs. At this higher temperature the process is transport controlled (see below Arrhenius plot in Fig. 7). Most gaseous precursor molecules are fast deposited and consumed just where they reach the hot surface first. Similar effects were observed in the CVD coating of nanorods where mushroom like structures were found at high deposition rates (Genduso et al., 2013).

For a detailed and quantitative discussion, the synopsis of the results for deposited mass, particle density, substrate coverage and particle size for the two substrate temperatures 110 °C and 230 °C (Fig. 4a and 4b) is helpful. After a short induction period until a stationary precursor concentration over the substrate has been built up, the deposition rates (slope of the mass curves) for both temperatures are rather constant for the first 5 or 6 min, respectively. In this period the deposition at 230 °C is about 6 times faster than at 110°C due to faster diffusion of educt molecules to the surface, faster decomposition reaction and faster diffusion of gaseous organic products away from the reaction site. Thereafter the rates increase considerably.

But why is the deposition strongly accelerated in both series after a certain time? A change of the flow mode by the increasing number of particles and therefore roughness was ruled out. The flow conditions (linear flow rate about 50 cm/min) indicate laminar flow where an increase in surface roughness does not have an influence on friction or heat transfer. However, instabilities in the flow field due to buoyancy might occur (Rayleigh-Benard convection) triggering a transition to turbulent flow. Assuming that the effect of surface roughness on deposition rate is in the same order of magnitude as on friction one can estimate that a wall roughness far beyond the particle height would be required to cause a significant effect on the near wall flow (Surek and Stempin, 2007). Therefore, the observed effect could be explained by an impact of the already formed Ag particles. This might result in a better adsorption of the precursor, a locally higher temperature due to much less heat emission of Ag than of the FTO (emissivity $\varepsilon_{Ag} \approx$ 0.01-0.03, (Committee, 2002) $\varepsilon_{FTO} \approx$ 0.38 (Yang et al., 2015)) or an autocatalytic effect. For the latter an exponential increase of the reaction rate is reported (Atkins and de Paula, 2010). The non-perfect exponential curves could be due to a superposition of several effects. The onset of the strong acceleration begins at very different coverage values, about 5 % for 110 °C and 50 % for 230 °C. That the lower deposition rate is more sensitive to the catalyst seems plausible.

The trend of the coverage, calculated from average particle diameter and density, goes to some extend parallel to the deposited Ag mass as it does not distinguish between size and density. The saturation of the coverage for the 230 °C sample after 7.5 min despite increase of both particle size and deposited mass (Fig. 3, 10 min and 15 min) is explained by partial multi-layer formation due to rare free substrate area, the fast process controlled by material transport and lack of time for a fitting crystalline orientation in the nucleation or small crystallite state.

The complete absence of much smaller particles and the narrow size distribution point to a pronounced Ostwald Ripening (OR), though in addition particle migration and subsequent coalescence (PMC) cannot be excluded. Preferentially very small particles undergo OR, losing smallest units or atoms which diffuse over the surface and attach to bigger ones. The remaining even smaller species shrink even faster and disappear completely. In contrast to PMC the growth is gradual and under a certain thermodynamic control leading to quite homogenous particle sizes. Thus, the energy of the complete system is improved. Many experimental and theoretical studies on OR of solid particles on substrates are reported. Sintering of immobilized nanoparticle catalysts for steam reforming and automotive exhaust conversion results in a loss of their activity by Ostwald ripening at 550 °C (Hansen et al., 2013). Sn clusters on Si(111) at 300 °C showed a pronounced trend to large interparticle distances during OR as our Ag NP film (Carlow and Zinke-Allmang, 1997). Such spatial ordering was explained as local ripening, a special case of OR comprising both, size and spatial distribution by self-similar evolution (Lifshitz and Slyozov, 1959). There

the diffusion gradient is developed between two neighbouring clusters resulting in the preferential elimination of near cluster pairs. We want to add the aspect that nuclei move much faster than particles and smaller particles faster than bigger ones. Particles "attract" coalescing nuclei from all directions. However, species close to another one have a reduced area of attraction; the smaller the distance, the more shielded and reduced is this area. Therefore, these particles grow more slowly and finally aggregate with a near neighbour.

For the higher temperature the particle size distribution is clearly wider (see standard deviation). Here, OR and PMC towards a relatively stable uniform size are partially outbalanced by the fast arrival of new material. This is confirmed by the different relative decreases in density from 0.5 min to 5 min which are 30% and 60% for 230 °C and 110 °C, respectively. The situation for solid NPs films is more complex than for colloidal particles. The latter are surrounded by only one liquid medium and their size is controlled by crystalline properties as well as kinetic factors, such as the competitive reactions of particle growth and shielding by stabilizer molecules (Fischer and Henglein, 1989). In contrast, for film particles also the interaction with the substrate (adsorption, wetting, lattice match etc.) plays an important role. Moreover, unlike for reactions in a vessel with limited educt, spray pyrolysis provides a continuous educt supply and is a complex action involving evaporation of solvent and precursor, material transport to and from reaction site, adsorption and decomposition.

What hinders the growth of bigger Ag NPs before all other small Ag NPs reach the same size? SEM cross-sections of a film with ~60 nm Ag NPs (see Fig. S1 in supplementary material) demonstrate a contact angle bigger than 90° indicating a repulsion from the FTO surface and a low free surface energy of the latter. Only in the first minutes the small species with high energy search a stabilization in substrate valleys, for the bigger, more stable particles the contact with the FTO is energetically not favoured anymore and the bigger a particle, the larger its contact area resulting in a preferential formation of new species which grow in average to just that size. Thus, the system energy is minimized. But more material is continuously added and the equilibrium of the system is readjusted according to Le Chatelier's principle. In other words, there is interplay between precursor concentration, material feed, the amount of already deposited material and of temperature.

As bad wetting and high surface tension let compact Ag films disintegrate into particles at about 200 °C, (Seweryn et al., 2013) these might reduce the driving force for coalescence also for our films at a certain stage. Moreover, then instead of forming a compact layer particles are created in a second level.

Influence of substrate temperature

The experiment series with two different temperatures shown above varied the deposition time to study its influence on the growth of Ag NPs. It is observed that the temperature also has a big effect. Therefore, a systematic study of the influence of the substrate temperature on the formation of Ag NPs is necessary. In this part, the samples were prepared at different substrate temperatures from 50 °C to 230 °C. Deposition time and precursor solution concentration were 5 min and 10 mM, respectively. The SEM images of these samples are shown in Fig. 5.

A few, small particles (marked by red circles) were formed already at temperatures as low as 50 °C and 70 °C, which is much lower than the reported temperature of 400 °C in common silver pyrolysis processes (Kumar et al., 2014; Pingali et al., 2005; Pluym et al., 1993; Shih and Chien, 2013). But merely with the substrate temperature of 80 °C or higher, a significant amount of Ag NPs can be deposited in a reasonable time. Only these samples with a statistically meaningful number of particles are considered for discussions of particle size, density and coverage. Both size and density of the formed particles are dramatically increased until a substrate temperature of 130 °C. Above this temperature only the density increases while

the particle size is practically constant, because the nucleation rate is higher. The higher nucleation rate and the first growth of the nuclei consume more material per time, thus limiting the particle size. The deposition rate now stagnates more or less because the process becomes feed rate limited (see below, paragraph "Deposition mechanism"). Moreover, there is no preference of the particle positions at edges and kinks observed above 110 °C. It could be explained by the high substrate temperature letting the general energy of the system overcome this preference (Bryant, 1977).

The deposited silver amount plotted in Fig. 4c is almost temperature independent in the range from 50 °C to 90 °C. Then up to 130 °C the increase is exponential. At the higher investigated temperature range up to 230 °C the deposited mass goes almost into saturation which might be due to the complete evaporation of the precursor material. Detail of the explanation can be found in the deposition mechanism part.

From the features shown above, simply by variation of deposition time and substrate temperature, the size and density of the obtained Ag NPs can be controlled. Fig. 6 gives a very interesting example. Different temperature / time parameters were used to obtain three samples, SEM images of which are shown in Fig. 6. The Ag NP film of Fig. 6a was obtained after 0.5 min deposition time at 110 °C substrate temperature. The Ag NPs have small particle size and low density. After 5 min at 230 °C the Ag NP film exhibits bigger particles with higher density (Fig. 6b). When we combine the deposition time of the first sample and the temperature of the second one, Ag NPs with roughly the size of one sample (Fig. 6a) and the density of the other (Fig. 6b) were produced (Fig. 6c). Details of the size and density of Ag NPs in Fig. 6 are shown in Table 1. Ag NPs with different other sizes and densities (coverage) can also be obtained by variation of deposition time and substrate temperature and keeping other deposition parameters constant. Size and coverage of those obtained Ag NPs are summarized in Fig. S2 in the supplementary material. When specific size and density of Ag NPs are required, the deposition parameters could be selected from Fig. S2. The substance shown in this paragraph demonstrates furthermore that particle size and density of Ag NPs can be controlled independently by the spray-CVD method.

Investigation of deposition mechanism

In addition to the control of size and density, the mechanism of the Ag NP deposition process is very important for understanding and further development of the method. In this part, the deposition mechanism is studied based on the results shown above as well as on a special kind of Arrhenius plot and classic experiments. A scheme of the deposition mechanism will summarize the results (Fig. 9).

Arrhenius plot. The deposited amount of silver within five minutes gives a deposition rate which can be used for the construction of an Arrhenius plot based on equation 1, where δ is the deposition rate, E_A the activation energy, R the universal gas constant, A the pre-exponential constant and T the substrate temperature.

$$\ln \delta = -\frac{1}{T}\frac{E_A}{R} + \ln A \qquad\qquad \text{Equation 1}$$

Plotting the logarithm of the deposition rate over the reciprocal temperature leads to the special kind of Arrhenius plot shown in Fig. 7. The deposition rate bases on the Ag to Sn ratio but not on the absolute deposition rate. However, as the Sn amount is constant in the commercial FTO substrates we can use it for relative considerations. The already discussed temperature series are used together with another series prepared with a 5 times higher precursor concentration of 50 mM resulting in a clearly higher deposition rate. Generally, in each series we can distinguish three sections. The first one is located in a temperature range from 50 to 80 °C, where the deposition rate of silver is very low and nearly constant. The second

section ranges from 80 °C to 130 °C (10 mM) or 110 °C (50 mM), respectively, where the deposition rate of Ag increases sharply with increase of substrate temperature. In the third section up to 230 °C, the slope is much smaller. The shape of the plots is typical for aerosol assisted chemical vapour deposition (AACVD) except for the incomplete evaporation regime in the beginning which is special and will be explained in the deposition mechanism paragraph below. However, it is hard to confirm the deposition mechanism by this plot alone. Therefore, classic experiments were carried out.

pH Experiments. Ethanol could have different benefits for the reaction, i.e., acting as a reducing agent for the silver precursor from Ag (I) to Ag (0) and/or improving its volatility by complex formation. For the former case, ethanol would get oxidized to formaldehyde or acetic acid. Therefore, to detect the by-products during the deposition of Ag NPs and study the role of ethanol in the deposition, two pH experiments were carried out. Details of the experiment design can be found in the experiment part. In general, for checking any volatile acid formation some Ag(hfacac)PMe$_3$ powder was placed in a glass tube and pH test stripes 10 cm away. Independently, whether pure nitrogen was blown over the dry Ag(hfacac)PMe$_3$ powder or ethanol saturated nitrogen over the precursor powder wetted with ethanol, upon heating to 150 °C the powder turns brownish and the pH stripes indicated acid evolution. Therefore, it is concluded that the (hfacac)PMe$_3$ ligand acts as reduction agent forming acidic decomposition products which agrees well with reported decomposition mechanism, but no evidence of the participation of ethanol in the redox reaction was obtained (Hampden-Smith and Kodas, 1995).

Decomposition Experiments. The During the deposition of In$_2$S$_3$ from ethanolic In(acac)$_3$ solution by ILGAR, it was shown by mass spectrometry that ethanol forms complexes with In(acac)$_3$ thereby enhancing the volatility dramatically (Gledhill et al., 2011). For the precursor material used in this work, a thermolysis temperature above 180 °C was reported (Dryden et al., 1993). However, the decomposition temperature of the precursor material in our work is much lower, i.e., 80 °C. Therefore, we wanted to investigate whether ethanol is responsible here for the extraordinarily low decomposition temperature of Ag(hfacac)PMe$_3$. Decomposition experiments with Ag(hfacac)PMe$_3$ precursor powder heated to 110 °C were used for studying the potential role of ethanol for enhancing volatility. For the first experiment, after pure N$_2$ flow for 30 min, the colour of the precursor material changed to brown and most of it seemed to melt. But a few centimetres away from the powder on the kapton tape, which fixes the copper block at the heater, there is nearly no change was observed. A significant difference was observed when ethanol saturated nitrogen was used (the second experiment). The melting and colour change of the precursor material occurred much faster than with pure nitrogen. In parallel, some visible vapour over the precursor was generated. After 30 min the kapton tape was covered with a dark brownish and mirror-like layer, obviously silver. Fig. 8 shows the tapes after the experiments. As a remark, the tapes didn't have direct contact with the precursor material. Thus, new volatile compounds were formed in the presence of ethanol above the precursor powder at a temperature lower than its melting point of 140-142 °C. The likely formed Ag complexes were transported by ethanol over a few centimetres through the gas phase to the kapton tape directly on the heater. There, the decomposition and the deposition of the Ag took place. The exact composition of the complex needs further investigation. However, the results give the strong evidence that at 110°C the process follows a CVD mechanism (Choy, 2003).

Deposition mechanism. Based on all the results shown above, the deposition mechanism was summarized in a scheme (Fig. 9). Evident from the Arrhenius plot, (Fig. 7) the mechanism is influenced by the substrate temperature. In the first section below 80 °C, the temperature is not high enough to evaporate the ethanol of the aerosol completely during the short residence time. Only a few little droplets can land on the substrate and the deposition rate is very low. Thus, the process is feed rate controlled and neither decomposition activation energy (E$_A$) nor evaporation enthalpy (ΔH$_{vap}$) play a role in the deposition since the precursor has

not been evaporated, i.e., there is nearly no slope observed. The mechanisms in this regime are the same for 10 mM and 50 mM series samples.

The second regime ranges from 80 °C to 110 °C for the 50 mM series samples, in which the solvent evaporates completely. Solid precursor particles arrive over the substrate and evaporate partly, while the rest remains solid (but with increasing temperature diminishing), do not adhere and are blown away by N_2 gas. The gaseous fraction was transported through the boundary layer, which separates the reaction zone over the substrate from the remaining reaction room, (Choy, 2003) adsorb and decompose on the substrate to form Ag nuclei or on existing particles to be integrated in, respectively. With increasing temperature the deposition rate is accelerated due to increase of both, precursor vapour pressure and decomposition rate. Still the evaporated material transported through the boundary layer is sufficient for the surface reaction. Thus, here the deposition rate is limited by both the evaporation rate of precursor material and the decomposition rate of the gaseous precursor material. Therefore, the slope is determined by ΔH_{vap} and E_A. For the 10 mM series, the mechanism of the second regime (80 °C - 130 °C) is different. Due to the low precursor material concentration, mainly the evaporation of precursor material limits the deposition rate. Hence, the slope of the second regime reflects mainly ΔH_{vap} of the precursor material and the slope is smaller than that of the 50 mM series samples.

The change to a smaller slope at 110 °C for the 50 mM series marks the start of the third section. Here, the precursor material is still not completely evaporated, but the surface reaction rate is high enough to decompose all the gaseous precursor material arriving on the substrate surface. Hence, in this range the overall deposition rate is transport controlled and the slope of the plot is mainly determined by ΔH_{vap}. (The contribution of the diffusion coefficient can be neglected). For the 10 mM series samples, the third section starts at around 130 °C and its slope is nearly zero. Due to the limited amount of precursor material, nearly all of it can be evaporated above the substrate and then transported to the substrate surface and decomposes there. Therefore, the feed-rate of precursor material limits the deposition rate and leads to the nearly zero slope of the deposition rate.

Generally, we predict that at even higher temperatures, the deposition rate will decrease due to the complete evaporation and as well as decomposition of precursor material and formation of Ag NPs already above the boundary layer. Only a few of those Ag NPs can land on the substrate and are easily blown away. (Choy, 2003; Kodas and Hampden-Smith, 1999)

Optical properties of Ag nanoparticles on FTO and related simulations

After the development of Ag NP films and studying the mechanism of the deposition process, we now investigate an application of Ag NPs. As mentioned before, the optical resonance bandwidth and position of Ag NP resonances is a very crucial property for applications (Atwater and Polman, 2010; Catchpole and Polman, 2008). To investigate the optical properties of Ag NPs deposited on FTO substrates, reflection and transmission were measured for three samples obtained from different deposition times, 1 min, 5 min and 7.5 min (precursor solution concentration was 10 mM and substrate temperature was 110 °C) as well as for the FTO substrate as a reference. The absorption of each sample was calculated as absorption = 100% - transmission - reflection (see Fig. 10b). Upper part SEM images of these four samples as well as average diameters and coverage of the Ag NPs obtained from SEM images are shown in Fig. 10a. The 16 nm Ag NPs (1 min deposition time) show a broad absorption band at around 420 nm wavelength. However, the band of the 21 nm Ag NPs (5 min deposition time) red shifts slightly to 430 nm and the absorption is stronger than for the 1 min Ag NPs sample. The absorption bands of the 16 nm Ag NPs and 21 nm Ag NPs at around 420 - 430 nm can be associated to the transverse plasmon resonance of small Ag NPs with nearly round shape and the red shift as well as stronger absorption can be due to the increase of particle size from 16 nm to 21 nm (Alonso et al., 2009; Mogensen and Kneipp, 2014). Due to the

absorption peak of FTO substrate at around 380 nm, the peaks at the same wavelengths for 16 nm Ag NPs and 21 nm Ag NPs could be attributed to the absorption of FTO substrate. The 39 nm Ag NPs (7.5 min deposition time) show two absorption bands, one at around 375 nm and the other at around 430 nm, which can be attributed to the non-spherical or complex shapes of the large particles (Schmid et al., 2014; Sherry et al., 2005; Wiley et al., 2007). The reason of the peak splitting can also be confirmed by the optical simulation shown in Fig. S3 in supplementary material, as when the shape of Ag NPs changes from sphere to non-spherical shape the peak splitting occurs. The absorption intensity is the highest of the three samples. This is due to the strong increase of both diameter and coverage. Mono dispersed Ag NPs (mentioned above) with similar resonance peaks have been widely used in different fields, especially for the generation of plasmonic near field which can benefit solar cells and other devices.

To study and predict the application of Ag NPs with certain size and coverage, simulation is a useful tool. In this case, Finite Element Method (FEM) simulations have been performed by COMSOL to estimate the theoretical absorption. Fig. 10c illustrates the optical structure used in the simulation. The shape of the Ag NPs used in the simulation was a cropped sphere. The sphere was cropped such that the height of the cropped object was 7/8 the diameter of the sphere, which was determined from a systematic variation of Ag NP's position above the substrate in simulation (see Fig. S3 in supplementary material). For all simulations periodic boundary conditions were used in the x-y plane, with the unit cell taking a hexagonal shape. Perfectly matched layer boundary conditions were used in the light propagation (z) direction. The material data for Ag was taken from Palik (Palik, 2012) while the FTO material data was obtained from fitting to measurements of our own samples (Phillip et al., 2014).

Fig. 10b shows the simulated absorption spectra of Ag NPs with the sizes and coverage given in Fig. 10a. It is observed that the absorption bands of all three samples in the simulated absorption spectra are at around 360 nm and 440 nm. It has to be mentioned that absorption peaks of 16 nm and 21 nm Ag NPs can be due to the enhanced absorption of FTO substrate because the sizes of these two samples are both very small. The absorption bands of the three samples at around 440 nm in simulation fit very well with the measured values. The simulated trend of absorption improvement with increasing particle size and coverage also matches well with the measured data. Although the main peak wavelength and trend fit well, two discrepancies between simulation and experimental spectra can be found: (1) the shorter wavelength absorption peaks of the three samples blue shifted 20 nm compared to the measured value; (2) there is an obvious peak splitting in the simulation. One possible reason is the actual height of the cropped Ag NPs in experiment is not always 7/8, and rather takes on a distribution of values not represented in the simulation. The other possible reason is the non-ideal spherical shape of Ag NPs in experiment. Roughness of FTO substrate which changed the incident angle of the light with respect to the substrate normal on Ag NPs may also contribute to the discrepancies. Simulations for different heights of Ag NPs, different shapes (sphere and irregular shape) as well as different incident angles of light have been carried out to study the possible reasons. Results of the simulations are shown in supplementary materials in Fig. S3, Fig. S4 and Fig. S5, respectively. It is observed in Fig. S3 that absorption peak splitting occurs when the height of Ag NP is smaller than the diameter. With the decrease of the height, the absorption peak at shorter wavelength blue shifts and the absorption becomes weaker while the absorption peak at longer wavelength red shifts and the absorption becomes stronger. The change of height of the Ag NP leads to the change of spherical shape and the different dimensions parallel and perpendicular to the interface define the two resonance peaks. From Fig. S4 we can see that the change of the shape of Ag NPs from spherical to irregular results in the decrease of absorption and changes the absorption peak shape. Fig. S5 shows that with deviation of light incidence from the normal, the absorption intensity increases and for larger angles (30 °) absorption peak position and shape change as well. Therefore, from the carried out simulations the possible reasons are confirmed. Fig. 10d shows an example (from simulation) of the near field generated by 39 nm Ag NPs at the wavelength of 360 nm. The generated near field can be used in different applications, i.e., in solar cells or in surface

enhanced Raman scattering. Above all, using a simplified model with parameters of Ag NPs extracted from experiments, the simulated absorption spectra fit well to the measured ones. Such a simulation can help predicting and understanding the potential of the application of plasmonic absorption and near field generated by Ag NPs.

The Ag NPs deposited by spray-CVD have been used in ultra-thin perovskite solar cells which leads to the relative enhancement of photocurrent and performance of about 22%, localized surface plasmon effect of the Ag NPs can be the reason for the enhancements (Liu et al., 2017). It is also expected that such Ag NPs can be used in more kinds of solar cells for the improvement of performance.

Conclusions

We have successfully developed a new method for the deposition of Ag NPs on FTO coated glass substrates based on an AACVD process with Ag(hfacac)PMe$_3$ as precursor, but the method is not limited to this substrate material. The required temperatures are tremendously lower than in previously reported work and can open new applications of such Ag NPs in heat sensitive systems. The manifold influences of the process parameters such as deposition time and substrate temperature were studied and explained in detail. By variation of the parameters, Ag NPs with independently controlled size and density can be obtained. It was found that a vapour phase formation takes place even at temperatures lower than the melting point of the precursor material. By simple experiments with the precursor powder a CVD mechanism involving the ethanol evidently explained the high volatility and low decomposition temperature of the precursor in our process. Three temperature sections are clearly distinguished by their slope in the Arrhenius plot. These are with increasing temperature for a high precursor concentration droplets regime (liquid-solid pyrolysis), kinetically controlled regime and transport controlled regime (both gas-solid pyrolysis), and for lower concentration droplets landing regime, feed rate limited regime (incomplete evaporation) and feed rate limited regime (complete evaporation), respectively. The respective determining energies such as evaporation enthalpy and activation energy could attribute to the particular Arrhenius slopes. For the growth of Ag NPs, the interplay between nucleation and growth by integration of fresh material or Ostwald Ripening are discussed with respect to narrow size distribution, absence of much smaller particles and quite homogenous distances to the next neighbours. In a pilot study for the application, the measured and simulated optical properties of the obtained Ag NP films were in good agreement and showed absorption peaks at the wavelength between 360 nm and 430 nm. Localized surface plasmon resonance of the obtained Ag NPs in this wavelength range is very promising for the absorption and performance enhancement of different kinds of solar cells. The obtained Ag NPs have been used for the photocurrent and performance enhancement of ultra-thin perovskite solar cells by such an effect, i.e., relative enhancements of 22%, and it is expected that Ag NPs deposited by spray-CVD can be used for improvement of the performance of several other kinds of solar cells. However, a complete understanding of all the complex chemical reactions and further applications of the Ag NPs need additional investigations.

Experimental part

The Ag NPs were deposited by a modified ILGAR (ion layer gas reaction) setup which is shown in Fig. 1. The complex salt Ag(hfacac)PMe$_3$ 99.9% purchased from Strem Chemicals was used as precursor. It was dissolved in absolute ethanol (Sigma Aldrich, 99.8%) and nebulized. The formed aerosol was carried by nitrogen gas to the FTO coated glass substrate (Solaronix) which lay on the heater. A flow rate of 1 L/min of the nitrogen gas was used in all depositions described in this work, as it gives the most homogenous particle films. Experiments were performed with precursor concentrations of 10 mM and 50 mM, and substrate temperatures from 50 °C to 230 °C. The deposition time was varied from 0.5 min to 15.0 min. After the finish of the deposition process, the nebulizer and the heater were stopped and air flow was used

inside the heater to cool down the temperature while the sample stayed on the heater under nitrogen carrier gas flow until the sample reached room temperature.

SEM was used to study the morphology, size, coverage and homogeneity of the deposited Ag NPs. SEM measurements were carried out on a Gemini Leo 1530 System equipped with a field emission gun and an in-lens detector. The size and density of the Ag NPs in each sample were extracted by ImageJ software from SEM images (magnification 20,000X) with an area of 1.50×1.04 μm^2. In this work, particle sizes refer to the diameters of the Ag NPs. Coverage of the Ag NPs was calculated using the determined size and density. For the different samples the considered number of particles ranged from 20 to 2854.

The deposited amount of silver was measured by LA-ICP-MS. Measurements were performed in multiline scan using a LSX213 laser system built by CETAC (laser wavelength 213 nm, 4 mJ/pulse, 20 Hz pulse frequency, spot size 200 μm, 100 μm/s scan speed for all samples). The NIST610 reference material was used for calibration.(Gundlach-Graham et al., 2015) This method is only able to provide element ratios. Therefore, the constant tin amount in the FTO layer was used as an internal standard. All values of silver amount given in this work are the molar ratio between silver and 10^6 tin.

To detect the by-products during the deposition of Ag NPs, another set up was used to indicate a possible formation of acid (pH experiments). A glass tube with middle part filled with Ag(hfacac)PMe$_3$ powder was placed in a heater. A wet pH test stripe (sensitivity range from pH 4.0 to pH 7.0) was placed into the end of the glass tube. During this experiment, the heaters were heated up to 150 °C. Both pure and ethanol saturated nitrogen gas was purged through the glass tube. Scheme of the pH experiment set up is shown in Fig. S6 in supplementary material.

In the decomposition experiments, the precursor material was placed on a clean FTO substrate located on the copper block of our standard set-up which was purged with a nitrogen flow rate of 1 L/min. The copper block was fixed on the heater using a kapton tape and kept at 110 °C for 30 min (see Fig. 1). In the first experiment, the Ag precursor powder was put on the substrate before heating and dry nitrogen flew over the powder. In the second experiment, the same amount of Ag precursor was put on the substrate but a droplet of ethanol was dripped on the powder and an ethanol saturated nitrogen flow was used. The nitrogen flow was obtained by bubbling the nitrogen through a washing bottle filled with ethanol. Other experiment parameters were kept constant. After each experiment, the kapton tape which was used to fix the copper block was removed and inspected.

Acknowledgements

Compliance with Ethical Standards

Conflict of interest: The authors declare that they have no conflict of interest.

References

Abou El-Nour KMM, Eftaiha Aa, Al-Warthan A, Ammar RAA (2010) Synthesis and applications of silver nanoparticles Arabian J Chem 3:135-140 doi:http://dx.doi.org/10.1016/j.arabjc.2010.04.008

Alonso JC, Diamant R, Castillo P, Acosta–García MC, Batina N, Haro-Poniatowski E (2009) Thin films of silver nanoparticles deposited in vacuum by pulsed laser ablation using a YAG:Nd laser Applied Surface Science 255:4933-4937 doi:http://dx.doi.org/10.1016/j.apsusc.2008.12.040

Atkins P, de Paula J (2010) Atkins' Physical Chemistry. OUP Oxford,

Atwater HA, Polman A (2010) Plasmonics for improved photovoltaic devices Nat Mater 9:205-213

Berhe TA et al. (2016) Organometal halide perovskite solar cells: degradation and stability Energy Environ Sci 9:323-356 doi:10.1039/C5EE02733K

Bryant WA (1977) The fundamentals of chemical vapour deposition Journal of Materials Science 12:1285-1306 doi:10.1007/bf00540843

Carlow GR, Zinke-Allmang M (1997) Self-Similar Spatial Ordering of Clusters on Surfaces during Ostwald Ripening Phys Rev Lett 78:4601-4604

Catchpole KR, Polman A (2008) Design principles for particle plasmon enhanced solar cells Appl Phys Lett 93:191113 doi:http://dx.doi.org/10.1063/1.3021072

Chen X et al. (2012) Broadband Enhancement in Thin-Film Amorphous Silicon Solar Cells Enabled by Nucleated Silver Nanoparticles Nano Lett 12:2187-2192 doi:10.1021/nl203463z

Choy KL (2003) Chemical vapour deposition of coatings Prog Mater Sci 48:57-170 doi:http://dx.doi.org/10.1016/S0079-6425(01)00009-3

Cobley CM, Skrabalak SE, Campbell DJ, Xia Y (2009) Shape-Controlled Synthesis of Silver Nanoparticles for Plasmonic and Sensing Applications Plasmonics 4:171-179 doi:10.1007/s11468-009-9088-0

Committee MPD (2002) ASM Ready Reference: Thermal properties of metals. ASM International,

Dryden NH, Vittal JJ, Puddephatt RJ (1993) New precursors for chemical vapor deposition of silver Chem Mater 5:765-766 doi:10.1021/cm00030a008

Ferry VE, Polman A, Atwater HA (2011) Modeling light trapping in nanostructured solar cells ACS Nano 5:10055-10064 doi:10.1021/nn203906t

Ferry VE et al. (2010) Light trapping in ultrathin plasmonic solar cells Opt Express 18:A237-A245 doi:10.1364/oe.18.00a237

Fischer C-H et al. (2011) The spray-ILGAR® (ion layer gas reaction) method for the deposition of thin semiconductor layers: Process and applications for thin film solar cells Sol Energy Mater Sol Cells 95:1518-1526 doi:http://dx.doi.org/10.1016/j.solmat.2010.12.019

Fischer CH, Henglein A (1989) Photochemistry of colloidal semiconductors. 31. Preparation and photolysis of cadmium sulfide sols in organic solvents J Phys Chem 93:5578-5581 doi:10.1021/j100351a049

Fu Y, Lu Y, Polzer F, Lux-Steiner MC, Fischer C-H (2016) In-situ Synthesis of Stabilizer-Free Gold Nanocrystals with Controllable Shape on Substrates as Highly Active Catalysts for Multiple Use Adv Synth Catal 358:1440-1448 doi:10.1002/adsc.201500848

Fu Y et al. (2013) Self-Assembled, Stabilizer-Free ZnS Nanodot Films Using Spray-Based Approaches J Phys Chem C 117:24632-24639 doi:10.1021/jp409054a

Genduso G et al. (2013) Deposition of very thin uniform indium sulfide layers over metallic nano-rods by the Spray-Ion Layer Gas Reaction method Thin Solid Films 548:91-97 doi:http://dx.doi.org/10.1016/j.tsf.2013.09.009

Gledhill S et al. (2011) The reaction mechanism of the spray Ion Layer Gas Reaction process to deposit In2S3 thin films Thin Solid Films 519:6413-6419 doi:http://dx.doi.org/10.1016/j.tsf.2011.04.131

Gundlach-Graham A, Dennis EA, Ray SJ, Enke CG, Barinaga CJ, Koppenaal DW, Hieftje GM (2015) Laser-ablation sampling for inductively coupled plasma distance-of-flight mass spectrometry J Anal At Spectrom 30:139-147 doi:10.1039/c4ja00231h

Hampden-Smith MJ, Kodas TT (1995) Chemical vapor deposition of metals: Part 1. An overview of CVD processes Chem Vap Deposition 1:8-23 doi:10.1002/cvde.19950010103

Hansen TW, DeLaRiva AT, Challa SR, Datye AK (2013) Sintering of Catalytic Nanoparticles: Particle Migration or Ostwald Ripening? Acc Chem Res 46:1720-1730 doi:10.1021/ar3002427

Kalfagiannis N et al. (2012) Plasmonic silver nanoparticles for improved organic solar cells Sol Energy Mater Sol Cells 104:165-174 doi:http://dx.doi.org/10.1016/j.solmat.2012.05.018

Kim S-S, Na S-I, Jo J, Kim D-Y, Nah Y-C (2008) Plasmon enhanced performance of organic solar cells using electrodeposited Ag nanoparticles Appl Phys Lett 93:073307 doi:http://dx.doi.org/10.1063/1.2967471

Kodas TTT, Hampden-Smith MJ (1999) Aerosol processing of materials. Wiley-Vch,

Kumar N, Alam F, Dutta V (2014) Deposition of Ag and Au–Ag alloy nanoparticle films by spray pyrolysis technique with tuned plasmonic properties J Alloys Compd 585:312-317 doi:http://dx.doi.org/10.1016/j.jallcom.2013.09.145

Lifshitz I, Slyozov V (1959) Kinetics of diffusive decomposition of supersaturated solid solutions Sov Phys–JETP 8:331-339

Liu Y et al. (2015) Phase transitions during formation of Ag nanoparticles on In2S3 precursor layers Thin Solid Films 590:54-59 doi:http://dx.doi.org/10.1016/j.tsf.2015.07.021

Liu Y et al. (2017) Enhancement of photocurrent in an ultra-thin perovskite solar cell by Ag nanoparticles deposited at low temperature RSC Advances 7:1206-1214 doi:10.1039/c6ra25149h

Masango SS, Peng L, Marks LD, Van Duyne RP, Stair PC (2014) Nucleation and Growth of Silver Nanoparticles by AB and ABC-Type Atomic Layer Deposition J Phys Chem C 118:17655-17661 doi:10.1021/jp504067c

Mock JJ, Barbic M, Smith DR, Schultz DA, Schultz S (2002) Shape effects in plasmon resonance of individual colloidal silver nanoparticles J Chem Phys 116:6755-6759 doi:http://dx.doi.org/10.1063/1.1462610

Mogensen KB, Kneipp K (2014) Size-Dependent Shifts of Plasmon Resonance in Silver Nanoparticle Films Using Controlled Dissolution: Monitoring the Onset of Surface Screening Effects J Phys Chem C 118:28075-28083 doi:10.1021/jp505632n

Moskovits M (2005) Surface-enhanced Raman spectroscopy: a brief retrospective J Raman Spectrosc 36:485-496 doi:10.1002/jrs.1362

Murphy M, Ting K, Zhang X, Soo C, Zheng Z (2015) Current Development of Silver Nanoparticle Preparation, Investigation, and Application in the Field of Medicine J Nanomater 2015:12 doi:10.1155/2015/696918

Nie S, Emory SR (1997) Probing Single Molecules and Single Nanoparticles by Surface-Enhanced Raman Scattering Science 275:1102-1106 doi:10.1126/science.275.5303.1102

Palik ED (2012) Handbook of Optical Constants of Solids. vol v. 1. Elsevier Science,

Pelton M, Aizpurua J, Bryant G (2008) Metal-nanoparticle plasmonics Laser Photonics Rev 2:136-159 doi:10.1002/lpor.200810003

Perednis D, Gauckler LJ (2005) Thin Film Deposition Using Spray Pyrolysis J Electroceram 14:103-111 doi:10.1007/s10832-005-0870-x

Phillip M, Guanchao Y, Martina S (2014) A method for calculating the complex refractive index of inhomogeneous thin films J Phys D: Appl Phys 47:205301

Pingali KC, Rockstraw DA, Deng S (2005) Silver Nanoparticles from Ultrasonic Spray Pyrolysis of Aqueous Silver Nitrate Aerosol Sci Tech 39:1010-1014 doi:10.1080/02786820500380255

Pluym TC, Powell QH, Gurav AS, Ward TL, Kodas TT, Wang LM, Glicksman HD (1993) Aerosols in Materials Processing Solid silver particle production by spray pyrolysis J Aerosol Sci 24:383-392 doi:http://dx.doi.org/10.1016/0021-8502(93)90010-7

Qian M, Li M, Shi X-B, Ma H, Wang Z-K, Liao L-S (2015) Planar perovskite solar cells with 15.75% power conversion efficiency by cathode and anode interfacial modification J Mater Chem A 3:13533-13539 doi:10.1039/C5TA02265G

Schmid M, Andrae P, Manley P (2014) Plasmonic and photonic scattering and near fields of nanoparticles Nanoscale Res Lett 9:50

Schmid M, Klaer J, Klenk R, Topič M, Krč J (2013) Stability of plasmonic metal nanoparticles integrated in the back contact of ultra-thin Cu(In,Ga)S2 solar cells Thin Solid Films 527:308-313 doi:http://dx.doi.org/10.1016/j.tsf.2012.12.023

Seweryn M, Manuel JM, Salvatore M, Francesca S, Francesco P, Isodiana C (2013) Self-assembled silver nanoparticles for plasmon-enhanced solar cell back reflectors: correlation between structural and optical properties Nanotechnology 24:265601

Sherry LJ, Chang S-H, Schatz GC, Van Duyne RP, Wiley BJ, Xia Y (2005) Localized Surface Plasmon Resonance Spectroscopy of Single Silver Nanocubes Nano Lett 5:2034-2038 doi:10.1021/nl0515753

Shih S-J, Chien IC (2013) Preparation and characterization of nanostructured silver particles by one-step spray pyrolysis Powder Technology 237:436-441 doi:http://dx.doi.org/10.1016/j.powtec.2012.12.032

Surek D, Stempin S (2007) Angewandte Strömungsmechanik: für Praxis und Studium. Vieweg+Teubner Verlag,

Teoh WY, Amal R, Madler L (2010) Flame spray pyrolysis: An enabling technology for nanoparticles design and fabrication Nanoscale 2:1324-1347 doi:10.1039/C0NR00017E

Valverde-Alva MA et al. (2015) Synthesis of silver nanoparticles by laser ablation in ethanol: A pulsed photoacoustic study Appl Surf Sci 355:341-349 doi:http://dx.doi.org/10.1016/j.apsusc.2015.07.133

van Lare C, Yin G, Polman A, Schmid M (2015) Light Coupling and Trapping in Ultrathin Cu(In,Ga)Se2 Solar Cells Using Dielectric Scattering Patterns ACS Nano 9:9603–9613 doi:10.1021/acsnano.5b04091

van Lare M, Lenzmann F, Verschuuren MA, Polman A (2012) Mode coupling by plasmonic surface scatterers in thin-film silicon solar cells Appl Phys Lett 101:221110 doi:http://dx.doi.org/10.1063/1.4767997

Wang Z, Rothberg LJ (2006) Silver nanoparticle coverage dependence of surface-enhanced Raman scattering Appl Phys B 84:289-293 doi:10.1007/s00340-006-2278-y

Wiley BJ, Chen Y, McLellan JM, Xiong Y, Li Z-Y, Ginger D, Xia Y (2007) Synthesis and Optical Properties of Silver Nanobars and Nanorice Nano Lett 7:1032-1036 doi:10.1021/nl070214f

Yang JK, Liang B, Zhao MJ, Gao Y, Zhang FC, Zhao HL (2015) Reference of Temperature and Time during tempering process for non-stoichiometric FTO films Sci Rep 5:15001 doi:10.1038/srep15001

Yin G et al. (2015) Integration of plasmonic Ag nanoparticles as a back reflector in ultra-thin Cu(In,Ga)Se2 solar cells Applied Surface Science 355:800-804 doi:http://dx.doi.org/10.1016/j.apsusc.2015.07.195

Yue L, Yan B, Attridge M, Wang Z (2016) Light absorption in perovskite solar cell: Fundamentals and plasmonic enhancement of infrared band absorption Sol Energy 124:143-152 doi:http://dx.doi.org/10.1016/j.solener.2015.11.028
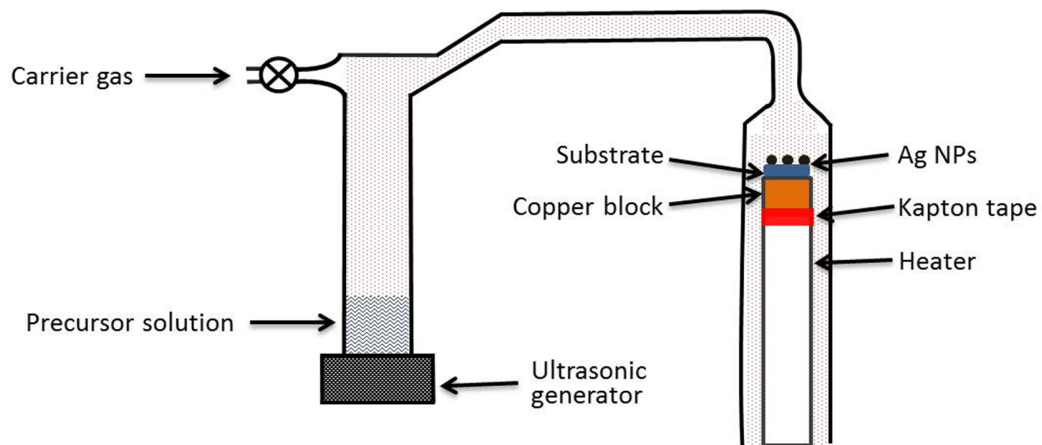
Fig. 1 Scheme of spray chemical vapour deposition set up used for Ag NP films deposition.
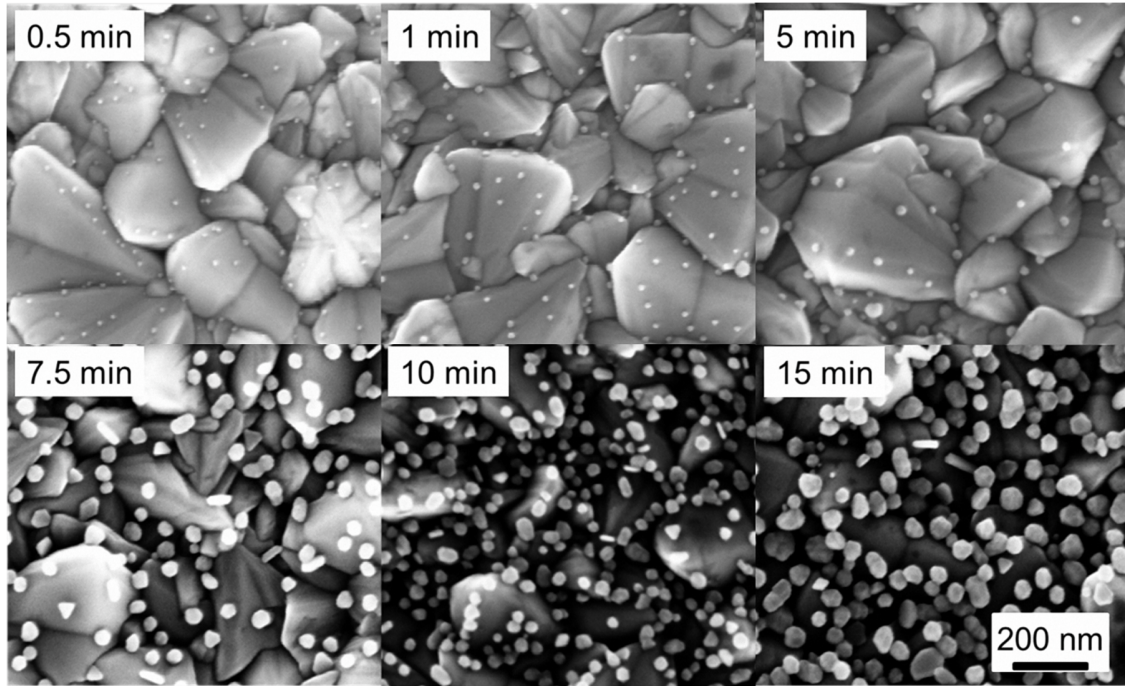
Fig. 2 SEM images of Ag NP films deposited with variation of deposition time (0.5, 1, 5, 7.5, 10 and 15 min). Precursor solution concentration and substrate temperatures were 10 mM and 110 °C, respectively.
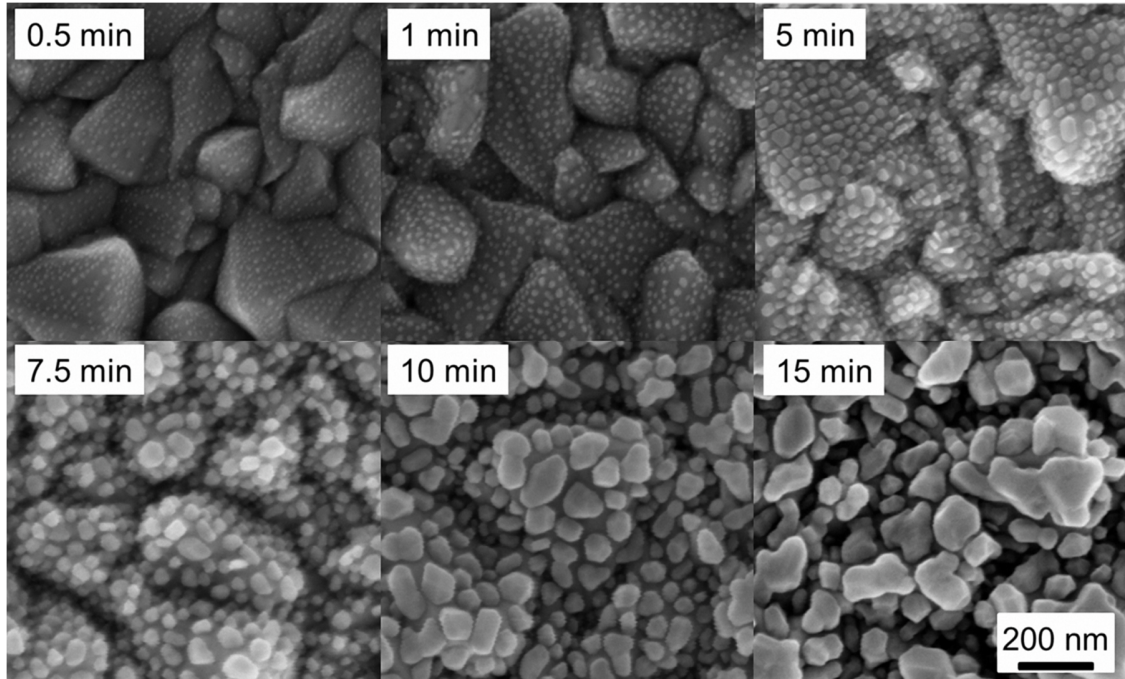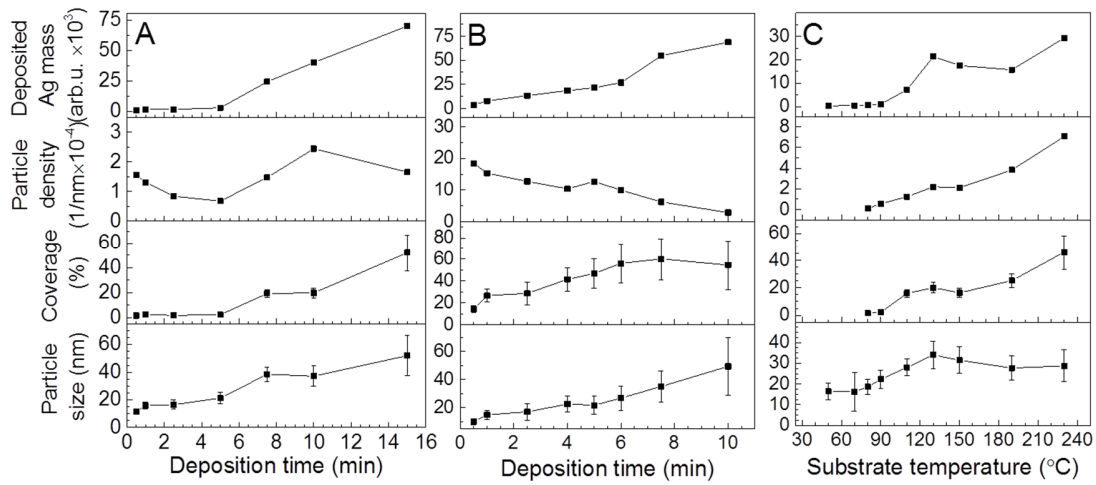
Fig. 3 SEM images of Ag NP films deposited with variation of deposition time (0.5, 1, 5, 7.5, 10 and 15 min). Precursor solution concentration and substrate temperatures were 10 mM and 230 ℃, respectively.

Fig. 4 Synoptic plots of crucial parameters of the obtained Ag NP films: deposited Ag mass, particle density, coverage and particle size. The error of deposited Ag mass is too small to visualize. Fig. 4a (extracted from Fig. 2) and Fig. 4b (extracted from Fig. 3) show the parameters dependent on the deposition time. Fig. 4c (extracted from Fig. 5) presents the parameters dependent on substrate temperatures.
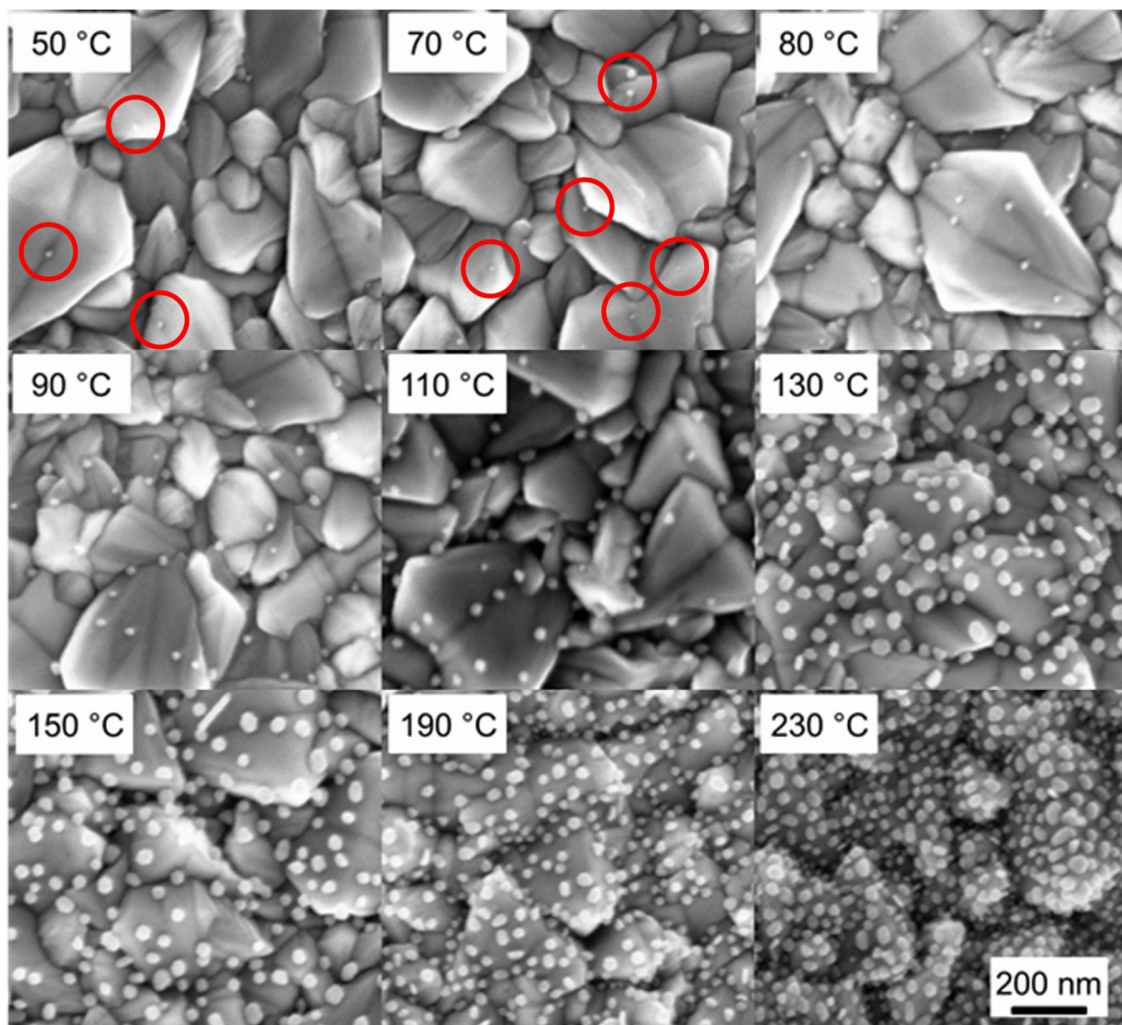
Fig. 5 SEM images of Ag NP films deposited with variation of substrate temperatures (50, 70, 80, 90, 110, 130, 150, 190 and 230 °C). Precursor solution concentration and deposition time were 10 mM and 5 min for the deposition of these samples.
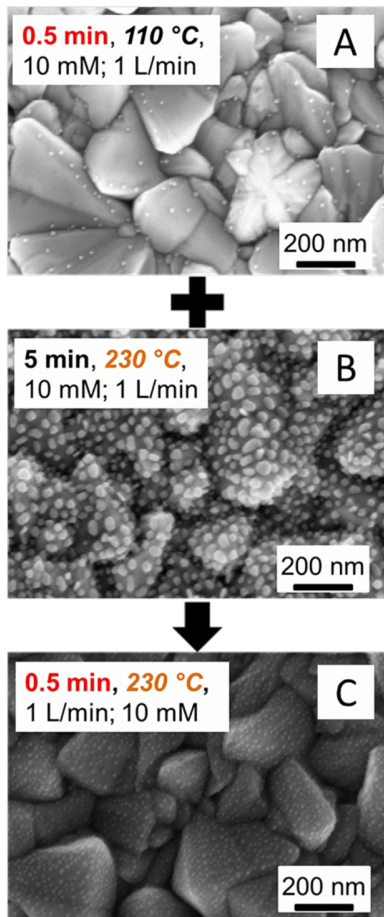
Fig. 6 SEM images of deposited Ag NP films using a precursor solution concentration of 10 mM in ethanol. Substrate temperature and deposition time were respectively, 110 °C and 0.5 min for (a), 230 °C and 5 min for (b), 230 °C and 0.5 min for (c).
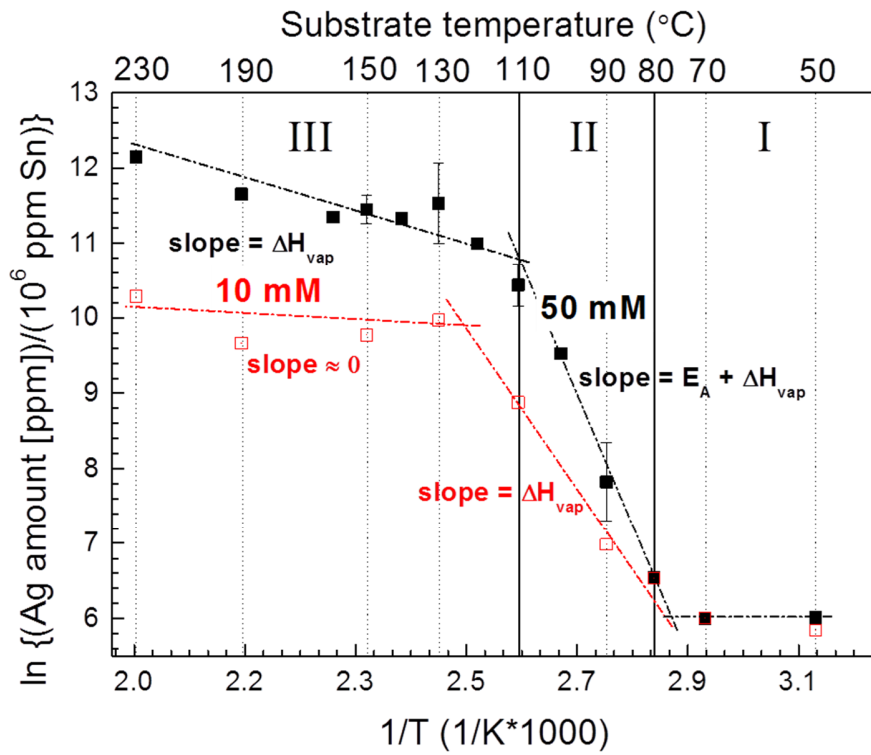
Fig. 7 Arrhenius plot of two series samples which were prepared with 10 mM and 50 mM precursor solution, respectively. Deposition time was 5 min for all the samples. Ag masses are relative values based on the internal standard Sn. The values of 90, 110, 130 and 150 °C samples were the average of two sample values and the errors were obtained accordingly. The errors of other samples are too small to visualize.
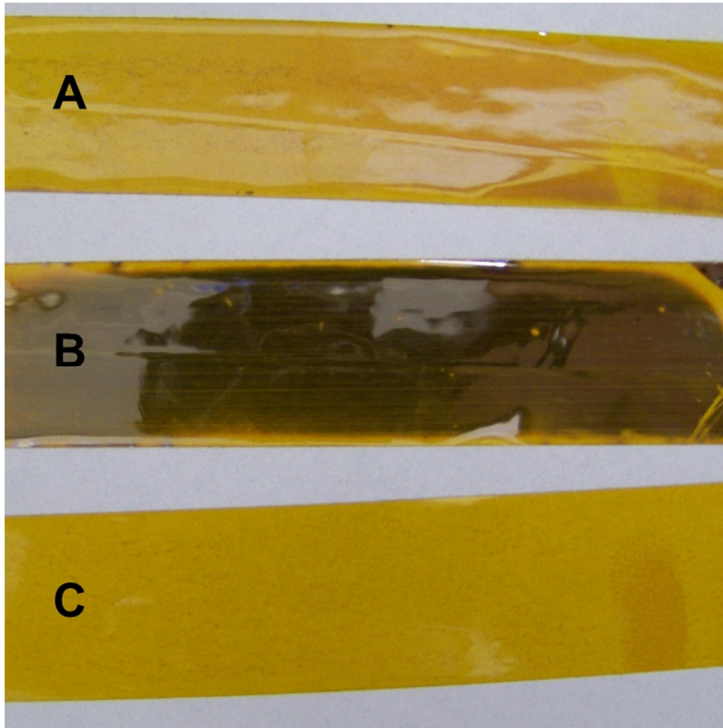
Fig. 8 Kapton tape stripes after the decomposition experiment of Ag(hfacac)PMe$_3$ powder. Fig. 9a and Fig. 9b show the tapes after experiment without and with ethanol, respectively. Fig. 9c shows the untreated reference tape.
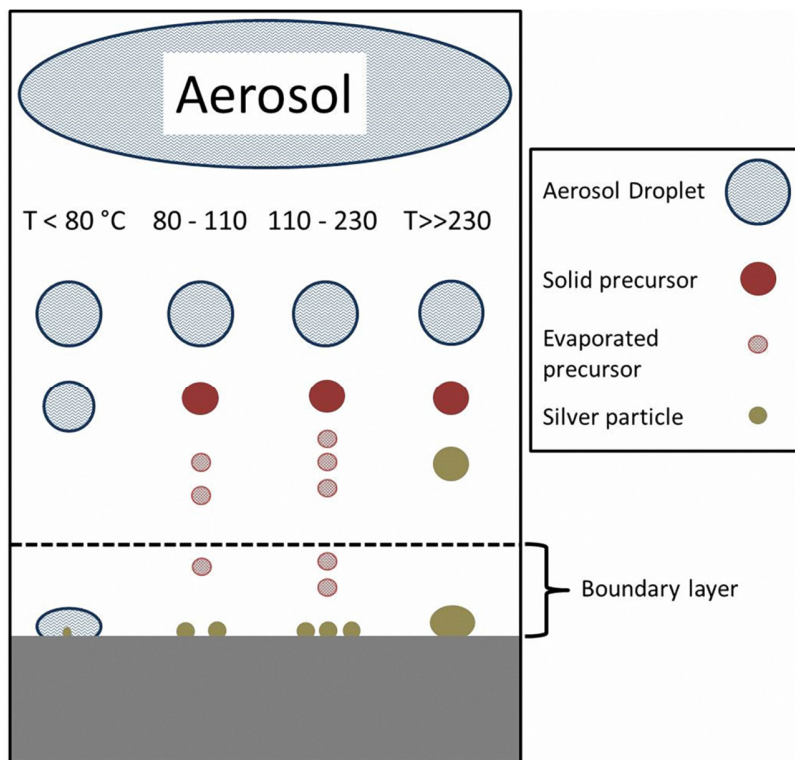
Fig. 9 Schematic illustration of the deposition mechanisms with variation of substrate temperature.
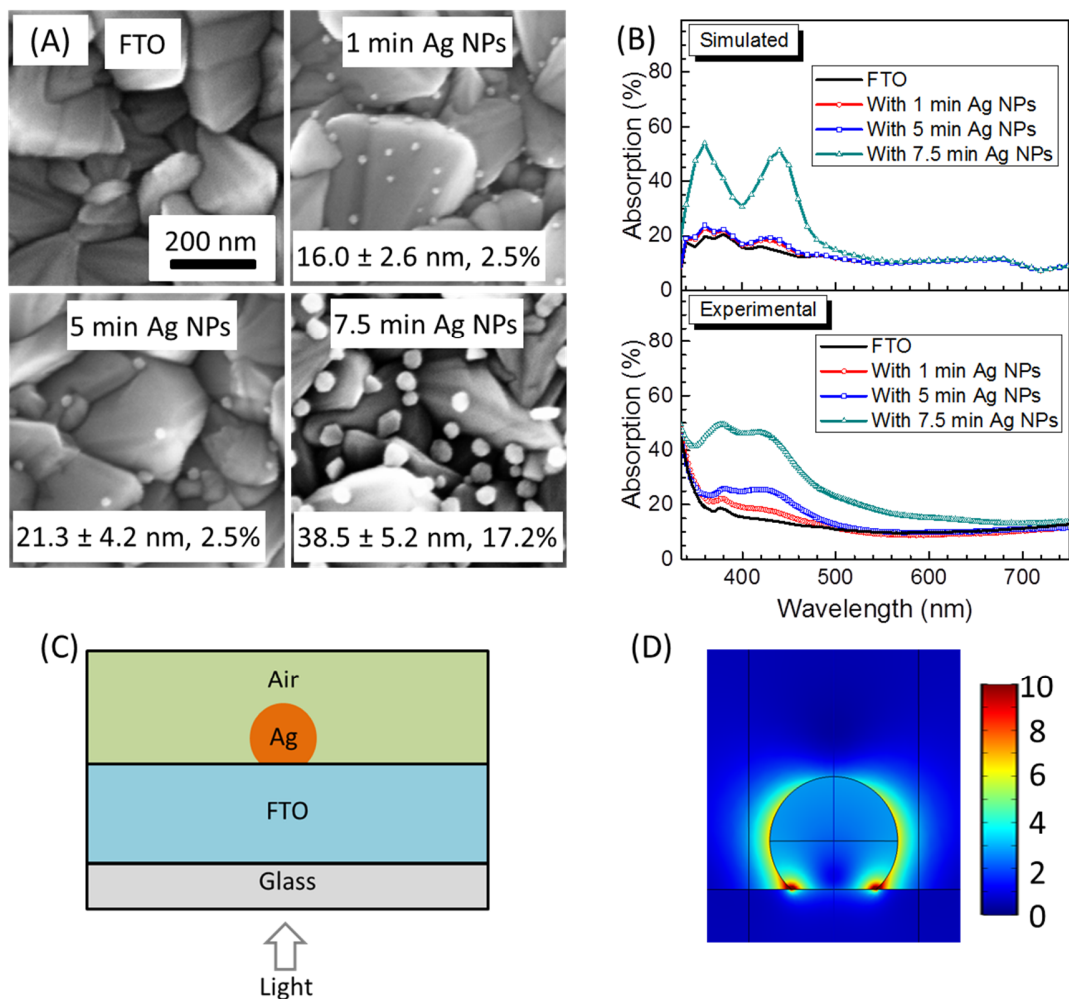
Fig. 10 (a) SEM images of Ag NPs obtained with 1, 5 and 7.5 min deposition time on FTO substrate. Substrate temperature and precursor solution concentration for Ag NPs deposition were 110 °C and 10 mM, respectively. Average diameters and coverage of Ag NPs calculated from SEM images which were used for the simulation are shown on the SEM images as well. (b) Measured and simulated absorption spectra of the samples shown in Fig. 10a. (c) Cross section of the Ag NPs on top of FTO layer system in the finite element method (FEM) simulation. (d) Simulated near field distribution (cross section) of the 7.5 min Ag NP at 360 nm wavelength.

Table 1 Average diameters and densities of Ag NPs calculated from SEM images shown in Fig. 6. Deposition time of the Ag NPs were 0.5, 5 and 0.5 min for the samples in Fig. 6a, Fig. 6b and Fig. 6c, respectively. Substrate temperatures for the three samples were 110, 230 and 230 °C, respectively. Precursor solution concentration for Ag NPs deposition was 10 mM.

Samples	Diameter of Ag NPs (nm)	Density of Ag NPs (nm^{-2})
Ag NPs in Fig.6a	11.4 ± 1.9	1.6×10^{-4}
Ag NPs in Fig.6b	21.7 ± 6.3	1.3×10^{-3}
Ag NPs in Fig.6c	9.9 ± 2.0	1.8×10^{-3}